Longitudinal Comparative Quantification of [^{18}F]RO948 and florzolotau (18F) PET in the TgF344-AD Rat Model.

Oscar Moreno

o.moreno@amsterdamumc.nl

CIC biomaGUNE, Basque Research and Technology Alliance (BRTA) https://orcid.org/0000-0001-6804-7970

Michael Schöll

Wallenberg Centre for Molecular and Translational Medicine, University of Gothenburg

Abraham Martín

5Achucarro Basque Center for Neuroscience, Science Park UPV/EHU

Jordi Llop

CIC biomaGUNE, Basque Research and Technology Alliance (BRTA)

Research Article

Keywords: Tau PET, [18F]RO948, florzolotau (18F), TgF344-AD rat, Longitudinal quantification

Posted Date: April 6th, 2026

DOI: https://doi.org/10.21203/rs.3.rs-9314329/v1

Additional Declarations: The authors declare no competing interests.

Abstract

Purpose

Tau PET (positron emission tomography) quantification in advanced AD (Alzheimer's disease) animal models remains insufficiently harmonized, particularly for recently developed tau tracers. Here, we compared the longitudinal performance and quantification of [^{18}F]RO948 and florzolotau (18F) PET in the TgF344-AD rat model to identify tracer-specific methodological constraints and robust outcome measures.

Methods

TgF344-AD and wild-type rats (n = 6–10) underwent dynamic PET-CT with [^{18}F]RO948 at 10, 14, 18, and 22 months and with florzolotau (18F) at 18 and 22 months. Quantification included regional SUV, SUVR, two-step reference tissue modelling (SRTM2), plasma radiometabolite analysis, and *in vitro* autoradiography. For florzolotau (18F), brainstem-based modelling was used to derive BP_{ND} and evaluate SUVR time windows.

Results

[^{18}F]RO948 showed progressively increasing late signal in cortex and cerebellum, together with skull uptake and plasma radiometabolites. Late-frame quantification was unreliable, and $SUV_{20–35}$ was selected as a pragmatic metric. However, [^{18}F]RO948 signal increased with age in both Tg and wild-type rats, showed limited genotype separation, lacked a valid reference region, and displayed a non-tau binding component *in vitro*. In contrast, florzolotau (18F) showed stable washout kinetics, no evidence of radio-defluorination, and marked group differences in tau-relevant regions. The brainstem supported SRTM2 modelling, while $SUVR_{65–90}$ strongly correlated with BP_{ND}, supporting its use as a practical semi-quantitative metric.

Conclusion

In our study, tau PET quantification in TgF344-AD rats was strongly tracer-dependent. While florzolotau (18F) provides a robust framework for longitudinal tau assessment in this model, the limitations of [^{18}F]RO948 substantially restrict the interpretability and use of this tracer.

1. INTRODUCTION

Tau pathology, characterized by intraneuronal aggregation of hyperphosphorylated tau into neurofibrillary tangles (NFTs), is a defining feature of Alzheimer's disease (AD) strongly associated with cognitive

decline and disease progression [1]. Tau positron emission tomography (PET) enables *in vivo* quantification of tau burden, allowing disease staging and therapeutic monitoring in clinical research [2–5]. While early-developed tau PET tracers were limited by substantial off-target binding and suboptimal kinetics, next generation tracers have demonstrated improved specificity and signal-to-noise characteristics [6, 7]. Among these, [^{18}F]RO948 and florzolotau (18F) (PM-PBB3, APN-1607) are increasingly used in both clinical and preclinical studies [8–18].

Because tau deposition is regarded as a progressive and continuous process, preclinical longitudinal PET studies are particularly well-suited to characterize its temporal evolution [19]. However, despite the increasing use of tau PET tracers, quantification strategies remain insufficiently harmonized in advanced AD models. Accurate quantification of tau PET signal in these models is essential for interpreting longitudinal changes and subsequent translation to human pathology. Semi-quantitative approaches in PET, such as SUVR, are widely used due to their practicality, yet their validity depends on a valid reference region with low, non-specific tracer binding [20]. Alternatively, kinetic modelling offers robust estimates of binding potential but requires plasmatic input function or reference tissue and dynamic imaging [21].

Preclinical models of AD provide a controlled platform to investigate methodological constraints under a longitudinal setting that are difficult to implement in humans. Among them, the TgF344-AD rat model, a double transgenic line expressing human amyloid precursor protein (APPsw) and human presenilin-1 (PSEN1ΔE9) mutations, develops age-dependent amyloidosis, spontaneous NFT-like hyperphosphorylated tau, neuroinflammation, and neuronal loss that closely recapitulate aspects of human AD pathology [22]. To date, tau pathology in TgF344-AD rats has only been investigated using one first-generation tau PET tracer [23]. Consequently, a longitudinal evaluation with more advanced tau tracers is warranted to provide an updated *in vivo* characterization of tau progression in this model.

In this study, we investigated the performance of [^{18}F]RO948 and florzolotau (18F) PET to assess tau deposition in the TgF344-AD rat model under a longitudinal setting. By integrating *in vivo* PET, image-derived metrics, reference-tissue modelling, and *in vitro* autoradiography, this work provides a practical methodological foundation to guide tracer selection and quantification strategy in future tau PET studies using this model.

2. MATERIALS AND METHODS

2.1. Animals

Animal experimentation was conducted in accordance with the European Council Directive 2010/63/EU at CIC biomaGUNE (San Sebastián, Spain) facilities and approved by the Institutional Animal Care and Use Committee (IACUC) at CIC biomaGUNE and Diputación Foral de Guipúzcoa (PRO-AE-SS-169). Female TgF344-AD rats (n = 18) were purchased from the Rat Resource and Research Centre (RRRC) (MO, US). Female wild-type F344 rats (n = 12) were purchased from Janvier Labs (France). Animals arrived at our facilities at the age of 11 weeks and were housed in groups of 2–3 per cage with individual

ventilation, environmental enrichment, constant access to food and water and a 12:12 hour cycle of light and dark. Imaging studies were performed at different ages (as defined below) during light phase of the light–dark cycle. Animal weights were recorded before each PET imaging session, during the longitudinal study.

2.2. Study design

The present study was part of a 24-month multi-tracer longitudinal PET study in TgF344-AD and wild-type rats, including [^{18}F]RO948 and florzolotau (18F) imaging sessions. Further details on the parallel imaging study are provided in Moreno et al. [24]. For the present analysis, rats were divided into two groups: Tg (TgF344-AD, n = 6–10) and WT (wild-type F344, n = 6–10), following previous studies (Figure S1; Table S1) [23]. The study design was guided by previous reports in the TgF344-AD rat model demonstrating elevated tau pathology from 6 months of age, with progression up to 16 months and little further increase beyond 26 months [22]. Following this, a 12-month longitudinal PET study (from 10 to 22 months of age) was considered appropriate to capture the period of reported tau pathology for our analysis. However, due to tracer availability, florzolotau (18F) PET was performed only at 18 and 22 months, whereas [^{18}F]RO948 PET was acquired at 10, 14, 18, and 22 months. In general, the same animals were scanned longitudinally, except those removed for tissue collection, reaching humane endpoints, or dying spontaneously (see Moreno et al. for details). At each time point, animals were scanned from the same daily tracer production; when this was not possible, a second production was performed the following day. No animal was scanned on two consecutive days. Female rats were used because of their higher susceptibility to pathology, lower body weight at older ages, and lower aggressiveness than males.

2.3. Longitudinal PET-CT studies

PET-CT studies were performed using β- (spatial resolution < 1 mm) and X-cube microsystems (Molecubes, Belgium) in rats from both Tg and control groups. [^{18}F]RO948 PET scans were performed at 10, 14, 18 and 22 months of age. Florzolotau (18F) PET scans were performed at 18 and 22 of age. In all cases, anaesthesia was induced with isoflurane (3.0–5.0%) in pure oxygen, and maintained during imaging studies at 1.5–2.0% of isoflurane in pure oxygen. Anesthetized animals were injected intravenously in the tail vein with a saline solution (max. 10% EtOH) of either [^{18}F]RO948 (4.3 ± 0.5 MBq) or florzolotau (18F) (4.4 ± 1.4 MBq) (Tables S2-S5). Dynamic PET acquisition (90 min) started immediately before injection (frames: 1×24 s, 4×6 s, 2×12 s, 2×18 s, 4×60 s, 4×300 s, 5×600 s, 1×852 s). Scans were acquired in list mode, single bed position, with a 100 mm field of view (nose to kidneys). A 5-min CT scan (40 kV, 140 μA) followed each PET scan. Images were reconstructed using OSEM-3D with corrections for randoms, scatter, and attenuation. Images were analysed using PMOD software (PMOD Technologies Ltd, Zurich, Switzerland). Volumes of interest (VOIs) (cortex, hippocampus, striatum, cerebellum, brainstem) were defined using the Schiffer-T2 MRI template (Figure S8). PET images were spatially normalized by re-slicing them to the Schiffer T2 MRI atlas. Time activity curves were obtained for each region and expressed as standardized uptake values (SUV). Whole-brain SUV images were generated by averaging individual scans within the selected time window. Uptake values were

summarized as mean and standard deviation (SD) for each brain region, time point and experimental group. Percent differences between groups were expressed relative to WT means, and longitudinal changes were calculated from all pairwise comparisons within each group.

2.4. Kinetic modelling

Dynamic florzolotau (18F) PET data were analysed using reference tissue modelling with the brainstem as the reference region. All kinetic modelling was implemented in MATLAB R2017b (The MathWorks, Natick, MA, USA). The apparent reference efflux constant ($k\prime_2$) was estimated in a data-driven manner with the Simplified Reference Tissue Model (SRTM) using 18-month TACs (kBq/cc) from cortex, hippocampus, cerebellum, and brainstem. To improve stability, $k\prime_2$ derivation was restricted to high signal-to-noise regions (cortex, hippocampus, cerebellum), pooling WT and Tg data. SRTM was fitted separately for each region and animal using nonlinear least squares to estimate R_1, k_2, and BP_{ND}. TAC convolution accounted for frame duration, with frame weighting proportional to the square root of frame length. For each fit, $k\prime_2$ was calculated as $k\prime_2 = k_2 / R_1$. Unstable fits were excluded, and the population-level $k\prime_2$ was defined as the robust median of all QC-passed estimates pooled across animals and regions. This fixed $k\prime_2$ was then used in two-step simplified reference tissue model (SRTM2) to estimate regional BP_{ND} from all scans (18 and 22 months, both groups). BP_{ND} was interpreted as reflecting specific tracer binding relative to the non-displaceable compartment, independent of tracer delivery or reference tissue uptake.

2.5. *In vitro* studies and radiometabolites analysis

A detailed description of the *in vitro* studies including brain tissue processing, autoradiography, AT8 immunostaining, and [^{18}F]RO948 radiometabolite analysis is provided in the Supplementary Information.

2.6. Statistical analysis

All statistical analyses of PET data were performed in R (version 4.5.1, R Core Team, Vienna, Austria). Due to the unbalanced repeated-measures design, linear mixed-effects models were fitted separately for each region, where group and age were included as fixed effects, and animal ID as a random intercept. Models were fitted using restricted maximum likelihood, with p-values computed using the Satterthwaite approximation. Estimated marginal means were used to perform post-hoc contrasts: (1) between-group comparisons (Tg vs. WT) at each age, and (2) within-group comparisons across ages. P-values were adjusted using the Holm method. Significance levels were defined as $p \geq 0.05$ (ns), $p < 0.05$ (*), $p < 0.01$ (**), $p < 0.001$ (***), and $p < 0.0001$ (****). Model assumptions were verified by inspection of residuals. Random slopes were not included due to the limited number of repeated measures. Pixel intensity values from autoradiography experiments were analysed using a two-tailed unpaired t-test with Welch's correction using GraphPad Prism 9 (GraphPad Software, CA, USA). Differences were concluded significant for p values < 0.05: * ($p < 0.05$), ** ($p < 0.01$), *** ($p < 0.001$) and **** ($p < 0.0001$).

3. RESULTS

3.1. Longitudinal [^{18}F]RO948 PET

To evaluate tracer performance *in vivo*, [^{18}F]RO948 PET was used at 10, 14, 18, and 22 months of age in Tg and WT rats. Mean time activity curves (TACs), expressed as SUV, were obtained in different brain regions at each time point for both groups (Fig. 1). TACs peaked at approximately 2 minutes post-injection across all regions, with clearance of the tracer appearing slower in older animals in both groups. In deeper brain regions (hippocampus, striatum, brainstem), values reached an equilibrium state around 60 minutes, whereas in cortical and cerebellar regions near the skull, TACs continued to rise between 60 and 90 minutes after administration. To minimize the impact of this artificial signal increase, mean SUV values were calculated from an earlier acquisition window ($SUV_{20–35}$ = 20–35 minutes post-injection) in all brain regions and time points (Table 1). The individual SUV values for each animal are found in Tables S6-13 of the Supporting Information. Brain $SUV_{20–35}$ PET images from both groups revealed homogenous [^{18}F]RO948 uptake in all cases except in the cerebellum, which consistently showed lower uptake compared to other regions (Fig. 2a). SUV analysis showed progressive increase in tracer uptake with age in both Tg and WT animals in most of the brain regions (Fig. 2b). In Tg animals, SUV values in classically tau-rich regions, such as the cortex and hippocampus, increased significantly over time from 10 to 22 months ($p = 0.00002$ and $p = 0.0001$, respectively), with effect sizes ranging from 50% to 60% difference (Table S14). A similar trend was observed in the striatum ($p = 0.0001$), while regions typically devoid of tau also exhibited higher uptake at older ages (cerebellum, $p = 0.0008$; brainstem, $p = 0.009$) compared to baseline (10 months). Interestingly, a significant age-dependent increase was also detected in WT animals in the cortex ($p = 0.0027$), hippocampus ($p = 0.0042$) and striatum ($p = 0.0007$), with SUVs increasing up to 60% from 10 to 22 months, but not in the cerebellum and brainstem. Between-group differences were only significant at 22 months of age in the cortex ($p = 0.005$), hippocampus ($p = 0.014$), striatum ($p = 0.036$), and cerebellum ($p = 0.049$) (Table S15). Across regions and ages, group differences ranged from 20% to 40%, except at 14 months, where almost no difference was observed between Tg and WT animals. To evaluate whether early-window quantification ($SUV_{20–35}$) adequately reflects later tracer retention in a tau-rich region, we compared $SUV_{20–35}$ with $SUV_{65–90}$ in the hippocampus, which is less affected by skull spill-in (Table S16-17). SUV calculated 65 to 90 minutes post-injection showed group differences only at 10 months of age ($p = 0.0246$) with a longitudinal signal increase at 22 months compared to baseline in Tg rats ($p = 0.0086$) (Fig. 2c) (Table S18-19). Correlation analysis demonstrated a strong positive association between $SUV_{20–35}$ and $SUV_{65–90}$ measurements in pooled data from both groups ($r = 0.86$, $p = 9.4 \times 10^{-20}$), although with systematic differences in absolute magnitude (Fig. 2d).

Table 1

SUV values in the longitudinal [^{18}F]RO948 PET study for Tg and WT animals at different time points calculated 20–35 minutes post injection (mean ± SD).

		Cortex		*Hippocampus*		*Striatum*		*Cerebellum*		*Brain stem*	
Age		WT	Tg	WT	Tg	WT	Tg	WT	Tg	WT	Tg
10 months	**N**	8	8	8	8	8	8	8	8	8	8
	SUV	0.49 ± 0.16	0.64 ± 0.08	0.51 ± 0.18	0.69 ± 0.09	0.49 ± 0.19	0.67 ± 0.09	0.40 ± 0.14	0.51 ± 0.05	0.51 ± 0.17	0.67 ± 0.07
14 months	**N**	9	10	9	10	9	10	9	10	9	10
	SUV	0.62 ± 0.09	0.65 ± 0.13	0.65 ± 0.08	0.65 ± 0.21	0.63 ± 0.09	0.71 ± 0.13	0.51 ± 0.08	0.42 ± 0.16	0.66 ± 0.08	0.57 ± 0.27
18 months	**N**	10	6	10	6	10	6	10	6	10	6
	SUV	0.66 ± 0.12	0.78 ± 0.07	0.74 ± 0.14	0.85 ± 0.09	0.70 ± 0.17	0.82 ± 0.08	0.49 ± 0.14	0.63 ± 0.05	0.66 ± 0.20	0.88 ± 0.10
22 months	**N**	6	6	6	6	6	6	6	6	6	6
	SUV	0.73 ± 0.08	0.97 ± 0.19	0.82 ± 0.10	1.10 ± 0.23	0.81 ± 0.11	1.03 ± 0.21	0.60 ± 0.05	0.81 ± 0.29	0.79 ± 0.12	1.02 ± 0.32

3.2. [^{18}F]RO948 off-target binding

Visual inspection of acquired full-body PET images revealed off-target signal in the skeleton of all animals after [^{18}F]RO948 administration, particularly at the end of the acquisition time (30 to 90 minutes post-injection) (Figure S9). Time–activity curves extracted from the skull exhibited a pattern similar to that observed in cortex and cerebellum, suggesting possible activity spill-in from bone to adjacent brain regions (Figure S10). Quantification of skull uptake in the 65–90 min window showed high SUV values across all ages and groups. Uptake differed significantly between Tg and WT animals at 10 months ($p = 0.0405$) and was increased at 14 months compared with baseline in Tg animals ($p = 0.0497$). An increasing trend in skull uptake was observed between 18 and 22 months in both groups (WT: +22.1%; Tg: +18.5%), although this did not reach statistical significance.

3.3. [^{18}F]RO948 metabolism

To assess *in vivo* [^{18}F]RO948 stability, radiometabolites were analyzed in plasma from young wild-type TgF344 rats (n = 2) to avoid additional blood sampling in aged longitudinal cohorts. Radio-HPLC at 15, 30, and 60 min post-injection identified a more polar early-eluting radiometabolite (1.9 min) relative to parent [^{18}F]RO948 (10.6 min; Figure S11a). Unchanged tracer accounted for ~ 75% of total plasma

radioactivity at 15 min, decreasing to ~ 45% by 60 min, indicating substantial metabolic degradation and reduced availability of intact [^{18}F]RO948 over time (Figure S11b).

3.4. [^{18}F]RO948 *in vitro* autoradiography

Given the limitations imposed by [^{18}F]RO948 metabolism *in vivo*, we next examined regional binding using *in vitro* autoradiography, thereby eliminating confounding metabolic effects. We first assessed whether [^{18}F]RO948 binds specifically to tau in this model by performing homologous blocking with non-radioactive RO948. In parallel, we used non-radioactive florbetaben (FBB), a known amyloid ligand, to evaluate potential cross-binding of [^{18}F]RO948 to Aβ in Tg tissue. Brain tissue from WT and Tg rats collected at the end of the study (22–23 months; n = 1 per group) was incubated with [^{18}F]RO948, and total binding and blockade were quantified in the cortex, hippocampus, cerebellum, and brainstem. Non-blocked autoradiograms showed homogeneous [^{18}F]RO948 binding in both Tg and WT tissue with some off-target binding in white matter rich areas (e.g., corpus callosum), with no explicit differences between groups (Fig. 3a). Pixel intensity values were comparable across regions within each group, with the exception of the brainstem in Tg tissue where abnormally high values were observed, due to the presence of hotspots, and therefore excluded from analysis (Figs. 3b-d) (Table S38). Homologous blocking with RO948 markedly reduced tracer binding across all examined regions in Tg, while significant displacement also occurred in WT tissue, which does not contain tau aggregates (Table 2). Calculated self-blocking percentages were higher in Tg tissue (CTX: +39.8%; HIPP: +34.7%; CB: +35.9%) than in WT tissue (CTX: +28.1%; HIPP: +29.1%; CB: +20.6%), consistent with a higher proportion of specific binding in Tg animals (Fig. 3e) (Table S39). In contrast, FBB blocking resulted in minimal displacement in Tg tissue, indicating negligible cross-binding of [^{18}F]RO948 to amyloid-β (Fig. 3f).

Table 2

[^{18}F]RO948 pixel intensity values (mean ± SD) at different regions under no blocking, RO948 blocking and FBB (florbetaben) blocking for both groups.

Tg	No block		RO948 block		FBB block	
	Mean	SD	Mean	SD	Mean	SD
Cortex	56.3	7.0	40.3	2.7	55.6	3.4
Hippocampus	54.0	6.4	40.1	3.5	52.9	3.4
Cerebellum	52.5	3.2	41.9	6.5	51.1	1.0
Brain stem	62.2	10.5	56.2	3.9	59.0	11.6

3.5. Longitudinal florzolotau (18F) PET

Florzolotau (18F) PET was conducted in TgF344-AD and WT rats at 18 and 22 months of age to evaluate tracer performance in a longitudinal setting. Mean time activity curves (TACs), expressed as SUV, were obtained in different brain regions at each time point for both groups (Fig. 4). Tracer uptake peaked

rapidly at approximately 1-minute post-injection, followed by a progressive washout reaching a near steady state from 60 to 90 minutes. Tg animals exhibited higher and sustained tracer retention in the hippocampus compared to other regions at both ages. In contrast, WT animals displayed lower overall uptake and faster washout kinetics across all regions, with almost no differences between brain areas at later time points. Across ages, Tg animals at 22 months showed increased late-phase florzolotau (18F) retention relative to 18 months, whereas WT animals showed similar TAC profiles at both time points. PET images obtained 65 to 90 minutes post-injection revealed marked cortical and hippocampal florzolotau (18F) uptake in Tg animals, with lower and uniform retention in control animals across regions (Fig. 5a). The corresponding individual SUV values for each animal are found in Tables S20-23 of the Supporting Information. Tracer uptake in Tg animals was age-dependant across all brain regions, with higher mean SUV at 22 months compared to 18 months in the cortex (+ 43%, $p < 0.0001$), hippocampus (+ 44%, $p < 0.0001$), striatum (+ 44%, $p = 0.0001$), cerebellum (+ 27%, $p = 0.002$) and brainstem (+ 22%, $p = 0.05$) (Fig. 5b) (Table S24). No significant differences were found in WT animals over time in any of the regions, which resulted in a significant contrast in florzolotau (18F) uptake between Tg and WT rats at both 18 and 22 months (Table S25). Differences between groups were particularly high in the cortex (18mo.; $p < 0.0001$, 22mo.; $p < 0.0001$), hippocampus (18mo.; $p < 0.0001$, 22mo.; $p < 0.0001$) and cerebellum (18mo.; $p < 0.0001$, 22mo.; $p < 0.0001$), and less pronounced in the striatum (18mo.; $p = 0.005$, 22mo.; $p < 0.0001$) and brainstem (18mo.; $p = 0.03$, 22mo.; $p = 0.0002$).

3.6. Validation of methods to quantify florzolotau (18F) uptake

Further analysis using the brainstem as a reference region allowed calculation of tissue to reference values ($SUVR_{BS}$) for each animal and time point (Table S26-29). SUVR curves increased over time in a region- and age-dependent manner in Tg rats and did not reach a plateau within 90 minutes, with the largest effects in the hippocampus and cortex, while WT animals showed relatively stable SUVRs (Fig. 6). SRTM2 was used as a standard method to elucidate florzolotau (18F) binding potentials (BP_{ND}) for each animal and time point (Table S32-35). The apparent efflux rate constant of the reference region was estimated as $k\prime_2$ = 0.0125 min^{-1} (IQR: 0.0015–0.0294 min^{-1}), based on SRTM fits to dynamic and pooled PET data acquired at 18 months of age (Figure S12). Regional BP_{ND} estimated with SRTM2 demonstrated region-specific patterns consistent with tracer retention characteristics (Table 3) (Figure S13). The relative delivery parameter ($R1$) remained comparatively stable across groups and ages, indicating that observed BP_{ND} differences were not driven by changes in tracer delivery or perfusion. To identify an optimal time window for the estimation of SUVR, we compared the correlation of BP_{ND} with SUVR at 25–45 min, 45–65 min, and 65–90 min (Fig. 6b) (Table 3). Across all regions, SUVR values strongly correlated with BP_{ND} values (Pearson $r > 0.89$) with a near-linear scaling between the two measures over the full dynamic range of tracer uptake. Correlations were stronger at later SUVR windows, while regression slopes deviated from the theoretical relationship BP_{ND} = SUVR – 1 in high-binding regions. Importantly, this relationship was not solely driven by between-group separation, as similar linear trends were observed when analysis was restricted to Tg animals,

confirming that SUVR tracks BP_{ND} within the pathological range (Figure S14). Kinetic analysis justified the use of $SUVR_{65-90}$ as the optimal parameter closest to BP_{ND} for semi-quantitative calculations with florzolotau (18F) PET. Longitudinal $SUVR_{65-90}$ values in TgF344-AD rats were age-dependant in the cortex ($p = 0.007$), hippocampus ($p = 0.0009$), and striatum ($p = 0.0009$), whereas wild-type animals showed comparatively stable values between 18 and 22 months (Fig. 6c) (Table S30). Genotype differences were evident in the cortex, hippocampus and cerebellum at 18 months (all $p < 0.0001$) and remained highly significant at 22 months in all cases (cortex and hippocampus: $p < 0.0001$; cerebellum: $p = 0.0001$) (Table S31). In contrast, differences in the striatum were only significant at 22 months ($p < 0.0007$).

Table 3

Quantification values obtained in the longitudinal florzolotau (18F) PET study. Mean ± SD values of SUV, SUVR, BP_{ND}, and R1 are shown by region, genotype, and age. SUVR values were calculated using the brain stem as reference in three different time windows indicated as time post-injection. BP_{ND} and R1 were estimated using SRTM2.

		Cortex		*Hippocampus*		*Striatum*		*Cerebellum*		*Brain stem*	
Age		WT	Tg	WT	Tg	WT	Tg	WT	Tg	WT	Tg
18 months	**N**	10	8	10	8	10	8	10	8	10	8
	SUV (20–35)	0.39 ± 0.08	0.71 ± 0.07	0.51 ± 0.10	1.11 ± 0.09	0.49 ± 0.10	0.66 ± 0.06	0.47 ± 0.10	0.79 ± 0.06	0.48 ± 0.09	0.62 ± 0.07
	SUVR (25–45)	0.69 ± 0.04	0.93 ± 0.09	0.99 ± 0.04	1.41 ± 0.11	0.97 ± 0.05	1.01 ± 0.05	0.85 ± 0.04	1.09 ± 0.08	-	-
	SUVR (45–65)	0.73 ± 0.05	1.05 ± 0.11	1.03 ± 0.05	1.63 ± 0.12	0.99 ± 0.05	1.05 ± 0.06	0.90 ± 0.05	1.18 ± 0.09	-	-
	SUVR (65–90)	0.80 ± 0.06	1.15 ± 0.15	1.06 ± 0.06	1.81 ± 0.16	1.01 ± 0.06	1.07 ± 0.06	0.98 ± 0.06	1.28 ± 0.10	-	-
	BP_{ND} mean	0.00 ± 0.00	0.25 ± 0.18	0.04 ± 0.05	1.36 ± 0.40	0.02 ± 0.03	0.07 ± 0.06	0.00 ± 0.00	0.25 ± 0.09	-	-
	R_1 mean	0.67 ± 0.07	0.72 ± 0.07	0.98 ± 0.03	0.95 ± 0.05	0.96 ± 0.05	0.92 ± 0.05	0.92 ± 0.10	0.96 ± 0.09	-	-
22 months	**N**	6	7	6	7	6	7	6	7	6	7
	SUV (20–35)	0.39 ± 0.10	1.01 ± 0.22	0.49 ± 0.11	1.60 ± 0.32	0.46 ± 0.10	0.96 ± 0.19	0.46 ± 0.12	1.01 ± 0.22	0.44 ± 0.13	0.76 ± 0.21
	SUVR (25–45)	0.77 ± 0.10	1.05 ± 0.12	1.02 ± 0.13	1.55 ± 0.10	1.02 ± 0.09	1.12 ± 0.09	0.91 ± 0.09	1.13 ± 0.15	-	-
	SUVR (45–65)	0.83 ± 0.10	1.23 ± 0.16	1.07 ± 0.09	1.89 ± 0.20	1.02 ± 0.10	1.23 ± 0.12	0.95 ± 0.09	1.26 ± 0.15	-	-
	SUVR (65–90)	0.91 ± 0.09	1.37 ± 0.20	1.15 ± 0.17	2.16 ± 0.24	1.08 ± 0.15	1.29 ± 0.12	1.06 ± 0.12	1.35 ± 0.17	-	-
	BP_{ND} mean	0.00 ± 0.00	0.70 ± 0.29	0.08 ± 0.12	2.55 ± 0.64	0.05 ± 0.11	0.32 ± 0.13	0.02 ± 0.04	0.41 ± 0.16	-	-

	R_1 mean	0.78 ± 0.16	0.76 ± 0.07	1.05 ± 0.16	1.02 ± 0.06	1.03 ± 0.12	0.96 ± 0.06	1.00 ± 0.19	0.94 ± 0.15	-	-

3.7. Florzolotau (18F) *in vitro* autoradiography

Brain tissue from Tg and WT rats collected at the end of the study (22–23 months; n = 1 per group) was incubated with florzolotau (18F), and total binding and blockade were quantified. Obtained autoradiographs revealed distinctive florzolotau (18F) binding in Tg brain sections, particularly in the cortex and hippocampus, while WT tissue presented homogenous and lower binding overall (Fig. 7a). Specific binding was noticeable in Tg under homologous blockade (non-radioactive Florzolotau blocking) in classically tau rich areas, including a binding reduction in the cortex (-25%, $p < 0.0001$) and the hippocampus (-30%, $p < 0.0001$), but also in the cerebellum (-16%, $p = 0.0216$) without significant displacement in the brainstem (Fig. 7b, 7e) (Table 4) (Table S40). Notably, modest but significant binding displacement was also detected in WT tissue in the cortex (-6%, $p = 0.0476$) and the hippocampus (-13%, $p = 0.0017$) (Fig. 7c). Quantification of pixel intensities confirmed higher tracer retention in Tg tissue compared to WT in the cortex ($p < 0.0001$), hippocampus ($p < 0.0001$), cerebellum ($p = 0.003$) and brainstem ($p = 0.0739$) under non-blocking conditions (Fig. 7d) (Table S41). Heterologous blocking with non-radioactive florbetaben resulted in only minimal displacement (< 10%) in Tg brain sections (Fig. 7f).

Table 4
Florzolotau (18F) pixel intensity values (mean ± SD) at different regions under no blocking, FLZ (Florzolotau) blocking and FBB (florbetaben) blocking for both groups.

Tg	No block		FLZ block		FBB block	
	Mean	SD	Mean	SD	Mean	SD
Cortex	153.6	4.7	114.9	4.2	139.7	12.8
Hippocampus	167.2	2.6	117.1	1.7	154.6	4.1
Cerebellum	128.5	4.6	108.0	3.0	126.8	1.9
Brain stem	119.7	4.7	123.0	11.1	135.1	0.9

4. DISCUSSION

In the present study, we provided a systematic evaluation of [^{18}F]RO948 and florzolotau (18F) PET quantification in the TgF344-AD rat model. The main findings of this comparison are summarized in Table 5. Our results demonstrate that quantification strategy is intrinsically constrained by tracer-specific properties, with direct consequences for the biological interpretation of longitudinal tau PET data. Differences in kinetic behaviour, metabolic stability, and binding specificity did not merely influence data quality, but fundamentally determined whether tau-related signal could be reliably separated from non-specific and age-dependent effects in this model.

Table 5

Summary table comparison between [^{18}F]RO948 and florzolotau (18F) quantification analysis.

KINETIC BEHAVIOUR			
Feature	**[^{18}F]RO948**	**Florzolotau (18F)**	**Evidence**
Early peak & washout	Rapid peak (0–2 min) and washout at 20 min	Rapid peak (0–1 min) and monotonic washout	Averaged SUV Time-activity curves
Late-phase stability	Activity increases in the cortex and cerebellum due to skull activity spill-in	Stable decline toward low plateau	Averaged SUV Time-activity curves
Pseudo-equilibrium window	Apparent late stability in selected regions, except cortex and cerebellum	Clear late window (65–90 min)	Averaged SUV Time-activity curves
REFERENCE REGION			
Feature	**[^{18}F]RO948**	**Florzolotau (18F)**	**Evidence**
Low-binding non-specific brain region	Cerebellum (but has specific binding *in vitro*)	Brainstem	SUV[(a)], autoradiography
Stability across age & genotype	Cerebellum stable in controls. Longitudinal drift in Tg animals	Brainstem stable with age but higher in Tg animals (possible spill-in from cerebellum)	Longitudinal SUV analysis
Suitability for SUVR	Not supported	Supported (brain stem as reference)	SUVR–BP_{ND} agreement (florzolotau (18F) only)
QUANTIFICATION			
Feature	**[^{18}F]RO948**	**Florzolotau (18F)**	**Evidence**
Primary metric measure	SUV (20–35 min). Measures tracer retention	$SUVR_{BS}$ (65–90 min). Measures tracer specific binding	Longitudinal SUV analysis + kinetic modeling
Kinetic modeling	Not feasible (no reference)	Valid and convergent (SRTM2)	Longitudinal SUV analysis + kinetic modeling
SUVR ↔ BP_{ND} relationship	Not applicable	Strong linearity (r ≈ 0.89–0.97)	Pearson (r) analysis
Sensitivity to modeling	Modeling N/A; SUV quantification sensitive	Low (robust to k_2' variation)	Fitting SUV window. Histogram of k_2'

KINETIC BEHAVIOUR		
assumptions	to time window (late frames confounded)	values derived from SRTM

METABOLISM & BINDING			
Feature	**[^{18}F]RO948**	**Florzolotau (18F)**	**Evidence**
Metabolites	One polar radiometabolite	Not analysed	Plasma radio-HPLC chromatograms
Radio-defluorination	Highly suspected	Not observed	Bone uptake
Specific binding	Displacement in all regions. Suspected mixed contributions (target + non-target)	Specific binding in cortex and hippocampus. Low displacement in cerebellum and brain stem	Autoradiography (Homologous blocking)
Off-target binding	Suspected in white matter structures	Suspected in white matter structures	Autoradiography (visual evidence, not quantified)
β-amyloid cross binding	Minimal (< 10%)	Minimal (< 10%)	Autoradiography (Florbetaben blocking)
LONGITUDINAL ANALYSIS			
Feature	**[^{18}F]RO948**	**Florzolotau (18F)**	**Evidence**
Disease contrast over time	Weak Tg–WT contrast (up to 40%)	Strong, region-specific progressive Tg–WT contrast (up to 80%)	Longitudinal PET data
WT stability	Weak. Longitudinal increase	Strong. Minimal longitudinal drift	Longitudinal PET data
PRACTICAL RECOMMENDATIONS			
Scenario	**[^{18}F]RO948**	**Florzolotau (18F)**	
Static protocol	Early window preferred (20–35 min), with limitations	Late window acceptable (65–90 min)	
Modeling	Not advised	Recommended (SRTM2)	
Best outcome metric	SUV	$SUVR_{BS}$ / BP_{ND}	
Risk of bias	Higher (skull spill-in, metabolism)	Low	
Ideal study type	Semi-quantitative longitudinal	Quantitative longitudinal	

Both [^{18}F]RO948 and florzolotau (18F) exhibited rapid brain delivery and comparable early uptake, although their late-phase kinetics diverged markedly. [^{18}F]RO948 showed progressively increasing signal in cortical and cerebellar regions, whereas florzolotau (18F) displayed a classical reversible profile with stable washout. Converging evidence from *in vivo* imaging and plasma analysis indicates that the abnormal late uptake observed with [^{18}F]RO948 in cortex and cerebellum was largely driven by radiometabolism and extracranial spill-in, consistent with radio-defluorination. The presence of skull uptake and its age-dependent increase further support this interpretation. Notably, off-target signal in skull and meninges has also been reported in some clinical PET studies with [^{18}F]RO948 [18, 25]. Importantly, these effects introduce a time-dependent bias that compromises late-frame quantification and limits the interpretability of conventional SUV-based metrics. As a consequence, [^{18}F]RO948 required a constrained quantification strategy based on an early static window ($SUV_{20–35}$), selected to minimize metabolic and spill-in confounds. However, this approach comes at the cost of biological specificity. Early SUV predominantly reflects tracer delivery and initial retention rather than equilibrium binding, and therefore represents a composite signal of limited value for isolating tau-specific deposition. Although $SUV_{20–35}$ correlated strongly with later quantification metrics ($SUV_{65–90}$) in the hippocampus, a region less affected by spill-in, it still compressed the dynamic range and cannot be considered quantitatively equivalent to late retention.

The absence of a valid reference region for [^{18}F]RO948 was an additional limitation for quantitative interpretation. Despite the low cerebellar uptake observed in both groups, the longitudinal drift detected *in vivo* together with the *in vitro* displacement seen in autoradiography indicate that cerebellar signal cannot be considered purely non-specific uptake, precluding its use for normalization. Under our experimental conditions, the binding profile of [^{18}F]RO948 was therefore heterogeneous. Although autoradiography showed clear tracer displacement in the cortex and hippocampus of Tg tissue, consistent with specific binding in tau-rich regions, significant homologous blockade in WT tissue revealed a substantial non-tau component. These findings suggest that [^{18}F]RO948 uptake *in vivo* reflects a mixture of tau-related and non-tau signal in this model. In addition, because control animals showed longitudinal drift across most brain regions *in vivo*, age-related changes in the non-tau [^{18}F]RO948 signal cannot be excluded. The identity of this off-target signal was not determined in our study; however, potential contributors may include other aggregated protein conformations with β-sheet-rich structures, for which tau PET ligands have shown affinity in some contexts [26]. Importantly, cross-binding to amyloid-β was excluded for both [^{18}F]RO948 and florzolotau (18F), as only minimal displacement was observed *in vitro*. Overall, these limitations were directly reflected in the performance of [^{18}F]RO948 PET for detecting tau pathology in the TgF344-AD model, where [^{18}F]RO948 $SUV_{20–35}$ increased with age in both Tg and WT animals and showed minimal group separation until late time points. This pattern indicates that $SUV_{20–35}$ is sensitive to age-related effects but lacks sufficient specificity to robustly differentiate tau pathology. Taken together, our data indicate that [^{18}F]RO948 $SUV_{20–35}$ PET provides a biologically ambiguous signal in the TgF344-AD model, where tracer-related

and methodological factors substantially confound the interpretation of longitudinal changes, thereby limiting its utility for tracking tau pathology.

In contrast, florzolotau (18F) PET supported a coherent and biologically interpretable quantification framework in TgF344-AD rats. Initial analysis of a suitable reference region suggested using the cerebellum, consistent with previous mouse studies. However, increasing cerebellar SUV in Tg rats, together with evidence of *in vitro* displacement, led us to exclude this region for normalization. Further studies are required to determine whether florzolotau (18F) uptake in the cerebellum of TgF344-AD rats reflects tau-specific binding, similar to that observed in late-stage human tauopathies, or instead represents off-target binding [27]. Alternatively, the brainstem showed negligible displacement *in vitro* and moderate longitudinal stability across groups *in vivo*, supporting its use for reference tissue modelling. It should be noted that elevated uptake in the cerebellum of Tg rats may lead to partial-volume spill-over into adjacent regions, including the brainstem, as suggested by the similar age-related SUV changes observed in both regions. While the use of the brainstem as reference region in this study is supported by combined *in vivo* and *in vitro* observations, the absence of tau pathology in this region has not yet been conclusively demonstrated in this model and therefore warrants further investigation.

In our study, the absence of a clear plateau in florzolotau (18F) SUVR time–activity curves indicated that full equilibrium was not reached within the scan duration. Linear graphical methods that rely on equilibrium assumptions, such as Logan reference analysis, previously used in florzolotau (18F) PET studies, were therefore considered inappropriate. Instead, nonlinear reference tissue modelling was applied. Binding potentials were estimated using the two-step simplified reference tissue model (SRTM2), which improves parameter stability by fixing the reference tissue efflux rate constant ($k\prime_2$) [28]. Based on literature, this approach is particularly advantageous for small-animal PET studies with limited scan durations and reduced signal-to-noise ratios, providing more robust BP_{ND} estimates, especially in low-binding regions [29]. In our study, fixed $k\prime_2$ estimates derived from pooled dynamic data were within the expected physiological range, and sensitivity analyses showed that moderate variation in $k\prime_2$ did not alter group or age effects. Together, these results support the suitability of the brainstem as a reference region for kinetic analysis and the stability of the SRTM2 modelling approach in the TgF344-AD model. In addition, the strong linear correlation between BP_{ND} and $SUVR_{BS}$ across all regions indicated that SUVR at 65–90 min provides a reliable surrogate for binding potential over the observed dynamic range. This strong linear relationship indicates preserved proportional scaling and regional contrast, supporting the use of $SUVR_{65-90}$ as a practical semi-quantitative measure of florzolotau (18F) binding. Overall, this strategy provides a useful balance between methodological robustness and experimental feasibility by reducing scan duration and interpretation complexity for future longitudinal studies in TgF344-AD rats. Under this framework, $SUVR_{BS}$ translated into a clear biological signal of florzolotau (18F) binding *in vivo*, with robust differentiation between Tg and WT animals, high sensitivity to longitudinal tau-related changes, and region-specific uptake consistent with the distribution of pathology *in vitro* (Figure S15). Importantly, the *in vivo* regional distribution is consistent with the initial description of the TgF344-AD model, in which age-dependent tauopathy was

reported in the cortex and hippocampus, supporting the biological validity of florzolotau (18F) PET in this setting [22]. The close agreement between *in vivo* PET, autoradiography, and immunostaining further supports the use of florzolotau (18F) $SUVR_{BS}$ to reflect tau distribution successfully in the TgF344-AD model, allowing reliable differentiation between pathological and age-related effects.

Several limitations should be considered in the present study. First, spatial normalization of PET images relied on a young rat MRI atlas, which may introduce minor registration biases in aged animals. Second, although radiolabelling procedures were performed under dark conditions, florzolotau (18F) photoisomers may still contribute to non-displaceable background signal in the brain, despite lacking tau-binding affinity. Lastly, *in vitro* studies were limited in sample size and should be interpreted as supportive rather than exhaustive evidence.

In conclusion, our study demonstrates that tau PET quantification in the TgF344-AD rat model is not tracer-agnostic, but critically dependent on tracer-specific kinetic and binding properties. While [^{18}F]RO948 requires constrained semi-quantitative approaches and yields limited specificity for longitudinal assessment, florzolotau (18F) supports both modelling-based and late-window semi-quantitative strategies with clear pathological sensitivity. These findings highlight that quantification strategy is not a neutral analytical step, but a determinant of how disease-related and age-related signals are represented in longitudinal PET studies.

Declarations

COMPETING INTERESTS

The authors have no relevant financial or non-financial interests to disclose.

ETHICS APPROVAL

Animal experimentation was conducted in accordance with the European Council Directive 2010/63/EU at CIC biomaGUNE (San Sebastián, Spain) facilities and approved by the Institutional Animal Care and Use Committee (IACUC) at CIC biomaGUNE and Diputación Foral de Guipúzcoa (Project: PRO-AE-SS-169).

FUNDING

This work was partially funded by Grants PID2023-148642OB-I00 and PID2020-117656RB-I00, funded by MCIN/AEI/ 10.13039/501100011033. O.M. received Grant PRE2019-089068 funded by MCIN/AEI/ 10.13039/501100011033 and by "ESF Investing in your future".

AUTHOR CONTRIBUTIONS

Oscar Moreno: Writing – review & editing, Writing – original draft, Methodology, Investigation, Formal analysis, Data curation, Conceptualization. **Michael Schöll**: Writing – Review & editing, Conceptualization, Funding Acquisition. **Abraham Martín**: Writing – Review & editing, Conceptualization, Supervision. **Jordi Llop**: Writing – review & editing, Supervision, Project administration, Funding acquisition, Conceptualization.

Acknowledgements:

The authors would like to thank Roche and Aprinoia for kindly providing the corresponding precursor and reference compounds for the radiolabeling of [^{18}F]RO948 and florzolotau (18F), respectively.

DATA AVAILABILITY

The datasets generated during and/or analysed during the current study are available from the corresponding author on reasonable request.

References

1. Moscoso A, Heeman F, Raghavan S, Costoya-Sánchez A, Van Essen M, Mainta I et al (2025) Frequency and Clinical Outcomes Associated with Tau Positron Emission Tomography Positivity. JAMA. https://doi.org/10.1001/jama.2025.7817
2. Chen SD, Lu JY, Li HQ, Yang YX, Jiang JH, Cui M et al (2021) Staging tau pathology with tau PET in Alzheimer's disease: a longitudinal study. Transl Psychiatry 11. https://doi.org/10.1038/s41398-021-01602-5
3. Schöll M, Lockhart SN, Schonhaut DR, O'Neil JP, Janabi M, Ossenkoppele R et al (2016) PET Imaging of Tau Deposition in the Aging Human Brain. Neuron 89. https://doi.org/10.1016/j.neuron.2016.01.028
4. Ossenkoppele R, van der Kant R, Hansson O (2022) Tau biomarkers in Alzheimer's disease: towards implementation in clinical practice and trials. Lancet Neurol. https://doi.org/10.1016/S1474-4422(22)00168-5
5. Villemagne VL, Doré V, Burnham SC, Masters CL, Rowe CC (2018) Imaging tau and amyloid-? proteinopathies in Alzheimer disease and other conditions. Nat Rev Neurol. https://doi.org/10.1038/nrneurol.2018.9
6. Leuzy A, Chiotis K, Lemoine L, Gillberg PG, Almkvist O, Rodriguez-Vieitez E et al (2019) Tau PET imaging in neurodegenerative tauopathies—still a challenge. Mol Psychiatry. https://doi.org/10.1038/s41380-018-0342-8

7. Okamura N, Harada R, Ishiki A, Kikuchi A, Nakamura T, Kudo Y (2018) The development and validation of tau PET tracers: current status and future directions. Clin Transl Imaging. https://doi.org/10.1007/s40336-018-0290-y
8. Lu J, Bao W, Li M, Li L, Zhang Z, Alberts I et al (2020) Associations of [18F]-APN-1607 Tau PET Binding in the Brain of Alzheimer's Disease Patients With Cognition and Glucose Metabolism. Front Neurosci 14. https://doi.org/10.3389/fnins.2020.00604
9. Liu FT, Lu JY, Li XY, Liang XN, Jiao FY, Ge JJ et al (2023) 18F-Florzolotau PET imaging captures the distribution patterns and regional vulnerability of tau pathology in progressive supranuclear palsy. Eur J Nucl Med Mol Imaging 50. https://doi.org/10.1007/s00259-022-06104-0
10. Miyamoto M, Okuyama C, Kagawa S, Kusano K, Takahashi M, Takahata K et al (2023) Radiation dosimetry and pharmacokinetics of the tau PET tracer florzolotau (18F) in healthy Japanese subjects. Ann Nucl Med 37. https://doi.org/10.1007/s12149-023-01828-x
11. Kawamura K, Hashimoto H, Furutsuka K, Ohkubo T, Fujishiro T, Togashi T et al (2021) Radiosynthesis and quality control testing of the tau imaging positron emission tomography tracer [18F]PM-PBB3 for clinical applications. J Label Comp Radiopharm 64. https://doi.org/10.1002/jlcr.3890
12. Smith R, Schöll M, Leuzy A, Jögi J, Ohlsson T, Strandberg O et al (2020) Head-to-head comparison of tau positron emission tomography tracers [18F]flortaucipir and [18F]RO948. Eur J Nucl Med Mol Imaging 47. https://doi.org/10.1007/s00259-019-04496-0
13. Kuwabara H, Comley RA, Borroni E, Honer M, Kitmiller K, Roberts J et al (2018) Evaluation of18F-RO-948 PET for quantitative assessment of tau accumulation in the human brain. J Nucl Med 59. https://doi.org/10.2967/jnumed.118.214437
14. Wong DF, Comley RA, Kuwabara H, Rosenberg PB, Resnick SM, Ostrowitzki S et al (2018) Characterization of 3 novel tau radiopharmaceuticals,11C-RO-963,11C-RO-643, and18F-RO-948, in healthy controls and in Alzheimer subjects. J Nucl Med 59. https://doi.org/10.2967/jnumed.118.209916
15. Honer M, Gobbi L, Knust H, Kuwabara H, Muri D, Koerner M et al (2018) Preclinical evaluation of 18F-RO6958948, 11C-RO6931643, and 11C-RO6924963 as novel PET radiotracers for imaging tau aggregates in Alzheimer disease. J Nucl Med 59. https://doi.org/10.2967/jnumed.117.196741
16. Leuzy A, Klein G, Ossenkoppele R, Mattsson N, Janelidze S, Palmqvist S et al (2020) Longitudinal [18 F]RO948 PET SUVR is associated with Aβ accumulation and baseline tau pathology. Alzheimer's Dement 16. https://doi.org/10.1002/alz.046474
17. Tagai K, Ono M, Kubota M, Kitamura S, Takahata K, Seki C et al (2021) High-Contrast In Vivo Imaging of Tau Pathologies in Alzheimer's and Non-Alzheimer's Disease Tauopathies. Neuron 109. https://doi.org/10.1016/j.neuron.2020.09.042
18. Leuzy A, Smith R, Ossenkoppele R, Santillo A, Borroni E, Klein G et al (2020) Diagnostic performance of RO948 F 18 tau positron emission tomography in the differentiation of alzheimer disease from other neurodegenerative disorders. JAMA Neurol 77. https://doi.org/10.1001/jamaneurol.2020.0989

19. Kimura T, Ono M, Seki C, Sampei K, Shimojo M, Kawamura K et al (2022) A quantitative in vivo imaging platform for tracking pathological tau depositions and resultant neuronal death in a mouse model. Eur J Nucl Med Mol Imaging 49. https://doi.org/10.1007/s00259-022-05898-3
20. Innis RB, Cunningham VJ, Delforge J, Fujita M, Gjedde A, Gunn RN et al (2007) Consensus nomenclature for in vivo imaging of reversibly binding radioligands. J Cereb Blood Flow Metab. https://doi.org/10.1038/sj.jcbfm.9600493
21. Lammertsma AA, Hume SP (1996) Simplified reference tissue model for PET receptor studies. NeuroImage 4. https://doi.org/10.1006/nimg.1996.0066
22. Cohen RM, Rezai-Zadeh K, Weitz TM, Rentsendorj A, Gate D, Spivak I et al (2013) A transgenic alzheimer rat with plaques, tau pathology, behavioral impairment, oligomeric Aβ, and frank neuronal loss. J Neurosci 33. https://doi.org/10.1523/JNEUROSCI.3672-12.2013
23. Chaney AM, Lopez-Picon FR, Serrière S, Wang R, Bochicchio D, Webb SD et al (2021) Prodromal neuroinflammatory, cholinergic and metabolite dysfunction detected by PET and MRS in the TgF344-AD transgenic rat model of AD: A collaborative multi-modal study. Theranostics 11. https://doi.org/10.7150/thno.56059
24. Moreno O, Fernández I, Plaza-García S, Padro D, Baz Z, Ramos-Cabrer P et al (2026) Longitudinal P2X7R and myelin PET reveal distinct neuroinflammatory and white matter signatures compared with TSPO PET and DTI-MRI in the TgF344-AD rat model. Neuroimage [Internet]. Academic Press; [cited 2026 Apr 2];327:121753. https://doi.org/10.1016/J.NEUROIMAGE.2026.121753
25. Smith R, Strandberg O, Leuzy A, Betthauser TJ, Johnson SC, Pereira JB et al (2021) Sex differences in off-target binding using tau positron emission tomography. Neuroimage Clin 31. https://doi.org/10.1016/j.nicl.2021.102708
26. Okamura N, Harada R, Furumoto S, Arai H, Yanai K, Kudo Y (2014) Tau PET Imaging in Alzheimer's Disease. Curr Neurol Neurosci Rep. https://doi.org/10.1007/s11910-014-0500-6
27. Tagai K, Ikoma Y, Endo H, Debnath OB, Seki C, Matsuoka K et al (2022) An optimized reference tissue method for quantification of tau protein depositions in diverse neurodegenerative disorders by PET with 18F-PM-PBB3 (18F-APN-1607). NeuroImage 264. https://doi.org/10.1016/j.neuroimage.2022.119763
28. Wu Y, Carson RE (2002) Noise reduction in the simplified reference tissue model for neuroreceptor functional imaging. J Cereb Blood Flow Metabolism Lippincott Williams Wilkins 22:1440–1452. https://doi.org/10.1097/01.WCB.0000033967.83623.34
29. Naganawa M, Gallezot JD, Li S, Nabulsi NB, Henry S, Cai Z et al (2024) Noninvasive quantification of [18F]SynVesT-1 binding using simplified reference tissue model 2. Eur J Nucl Med Mol Imaging 52. https://doi.org/10.1007/s00259-024-06885-6

Figures

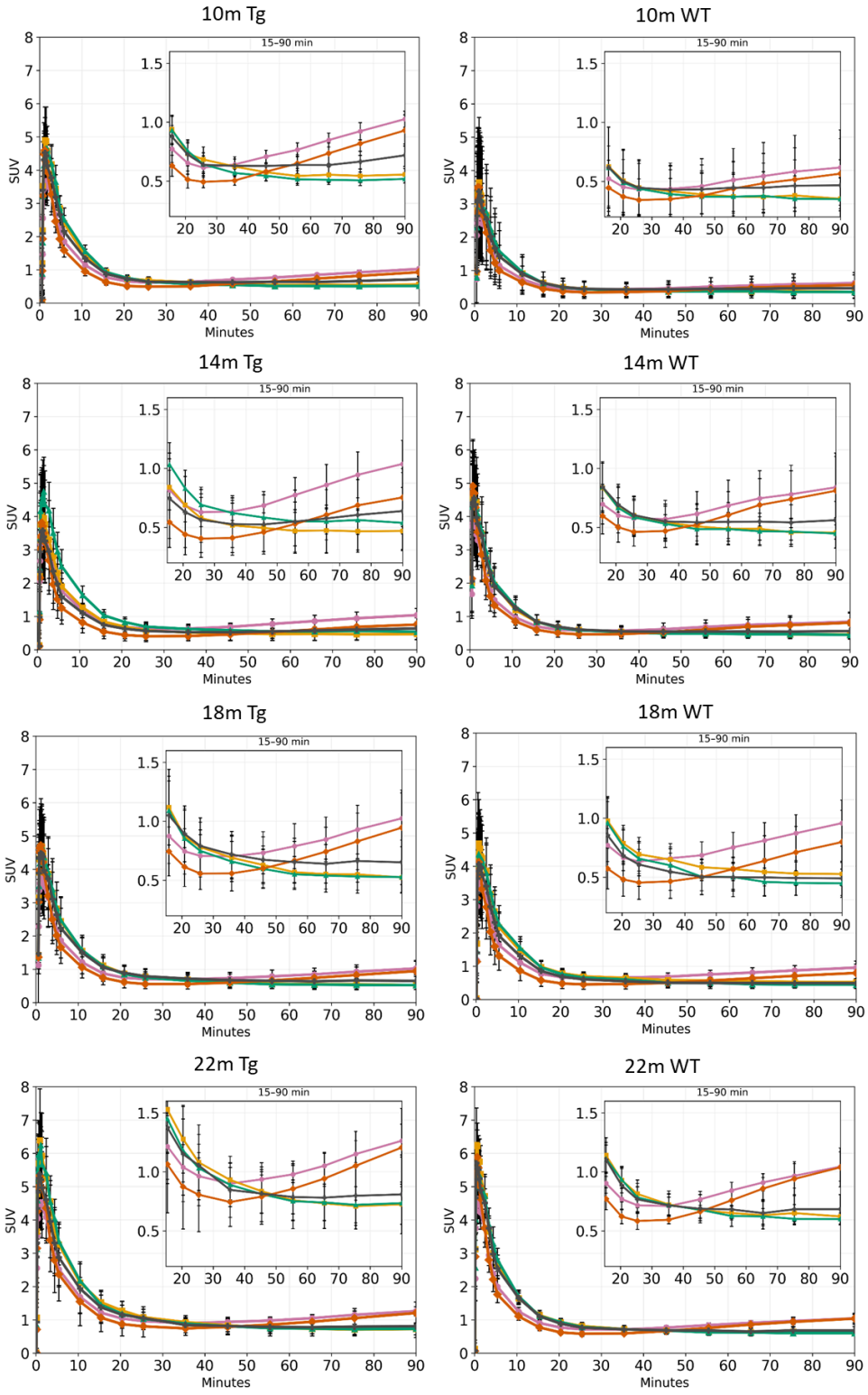

Figure 1

Averaged SUV time activity curves (TACs) in the longitudinal PET study of [^{18}F]RO948 for Tg and WT animals at 10, 14, 18 and 22 months of age. Inner graphs show a close-up of TACs between 15 and 90-min scan time. Cortex (pink), hippocampus (yellow), striatum (green), cerebellum (orange), brainstem (grey).

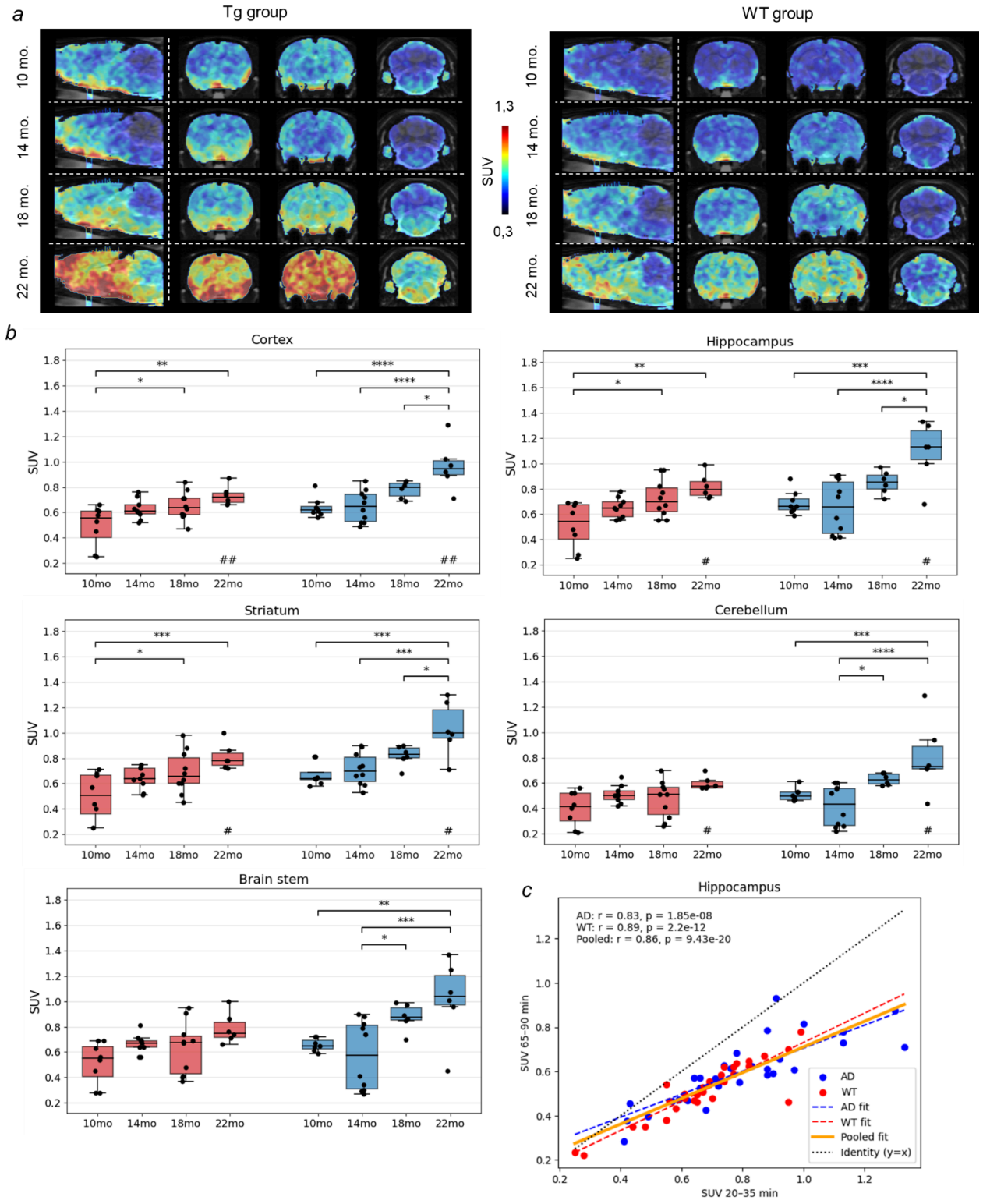

Figure 2

a) Longitudinal [^{18}F]RO948 SUV PET images obtained 20-35 min after injection in the Tg group and the WT group. Images correspond to the averaged PET image per time point and group (n = 6-10). b) SUV values in different brain regions for both animal groups (Tg: blue and WT: red) 20 to 35 min after tracer injection. Dots indicate individual animals. Stars (*) indicate statistical significance between time points within Tg or WT animals. Hash (#) indicates statistical significance between groups at each time point

(*p, #p < 0,05; **p, ##p < 0,01; ***p, ###p < 0,001; ****p, #### < 0.0001). c) Correlation between SUV 20–35 and SUV 65–90 in the hippocampus for WT (red) and Tg (blue) animals. Dashed lines represent group-specific linear regressions; the solid orange line indicates the pooled regression fit; the dotted black line represents the line of identity (y = x). Pearson correlation coefficients (r) and corresponding p-values are shown for each group and for pooled data.

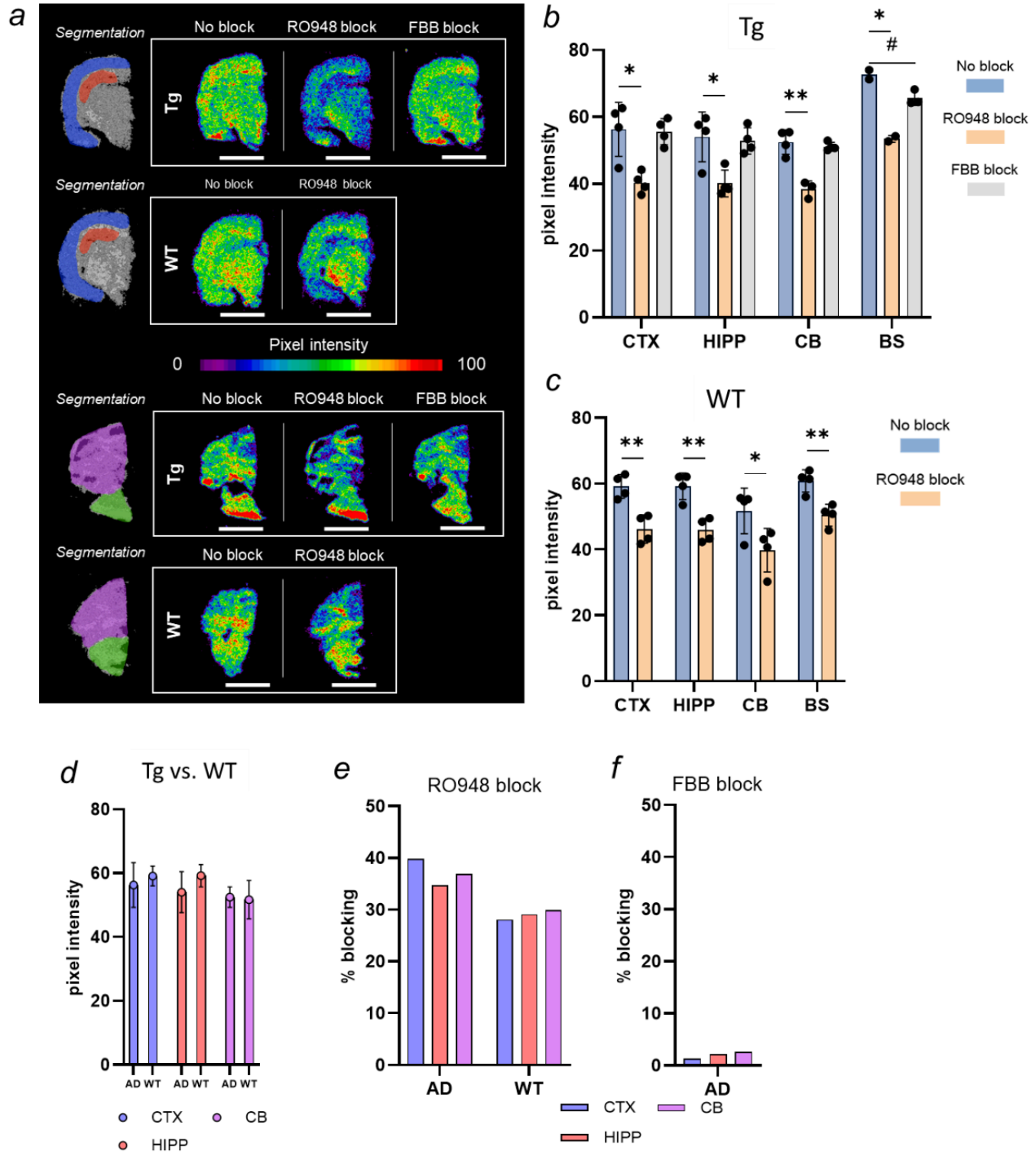

Figure 3

a) Representative coronal *in vitro* autoradiography images with [^{18}F]RO948 in Tg tissue (23 months, n =1) and WT tissue (22 months, n = 1). Manual segmentation is shown for clarity containing cortex (CTX, blue), hippocampus (HIPP, red), cerebellum (CB, purple) and brain stem (BS, green). Next to each slice is the corresponding blocked tissue: RO948 block and FBB block (FBB: Florbetaben). Scale bar = 3 mm. Bar plots show tracer binding (mean pixel intensity values) in each region in different conditions: no blocking, RO948 blocking and FBB blocking for Tg (b) and WT tissue (c). Dots indicate experimental replicates with the same brain. Stars (*) indicate differences between no block and RO948 block. Hash (#) indicates differences between no block and FBB block. d) Differences in mean pixel intensity values (no block) between Tg and WT tissue. Bar plot showing the percentage of blocking (%) in each group and region for RO948 self-blocking (e) and FBB blocking (f). */#p < 0,05; **p < 0,01.

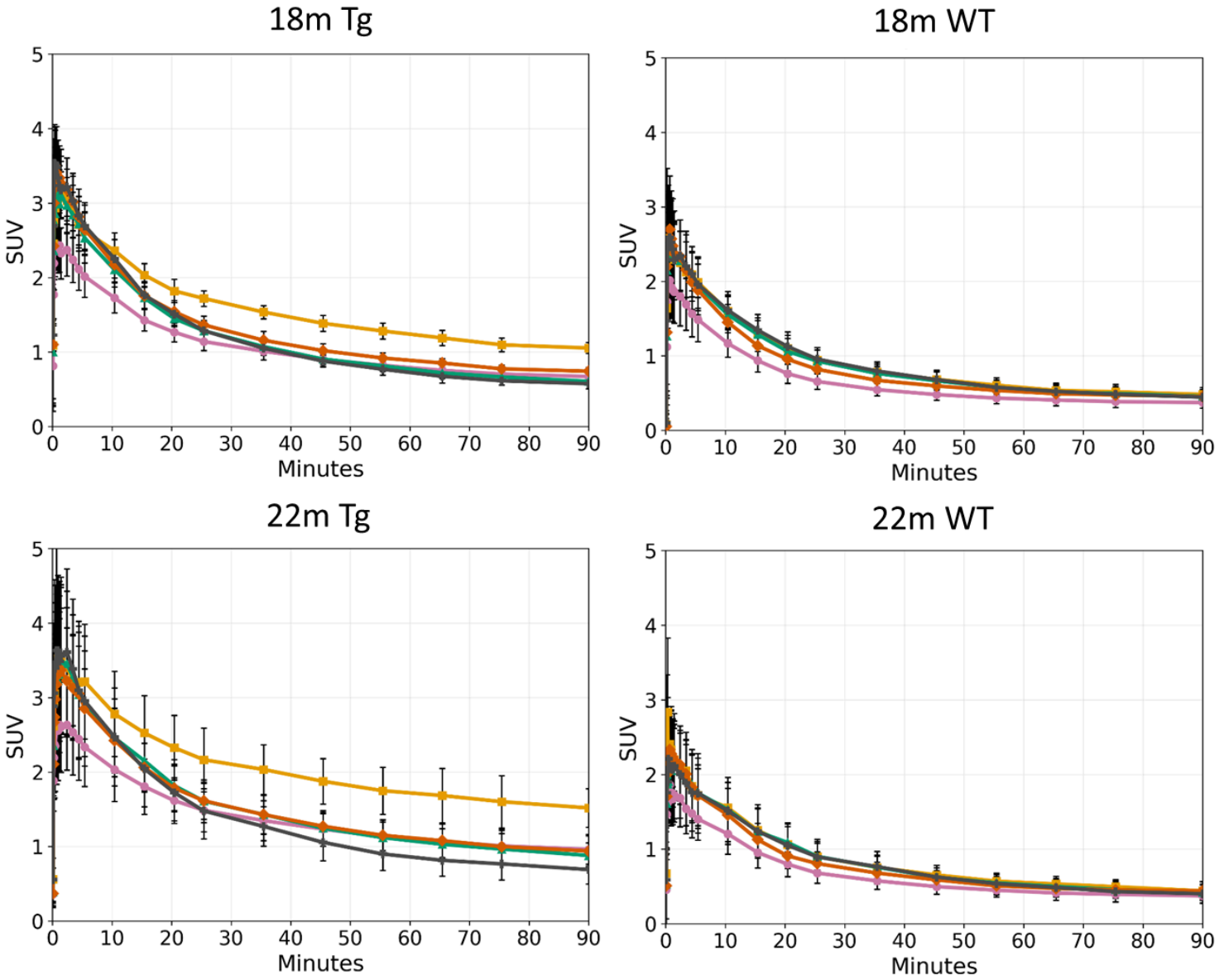

Figure 4

Averaged SUV time activity curves (TACs) in the longitudinal PET study of florzolotau (18F) for Tg and WT animals at 18 and 22 months of age. Cortex (pink), hippocampus (yellow), striatum (green),

cerebellum (orange), brainstem (grey).

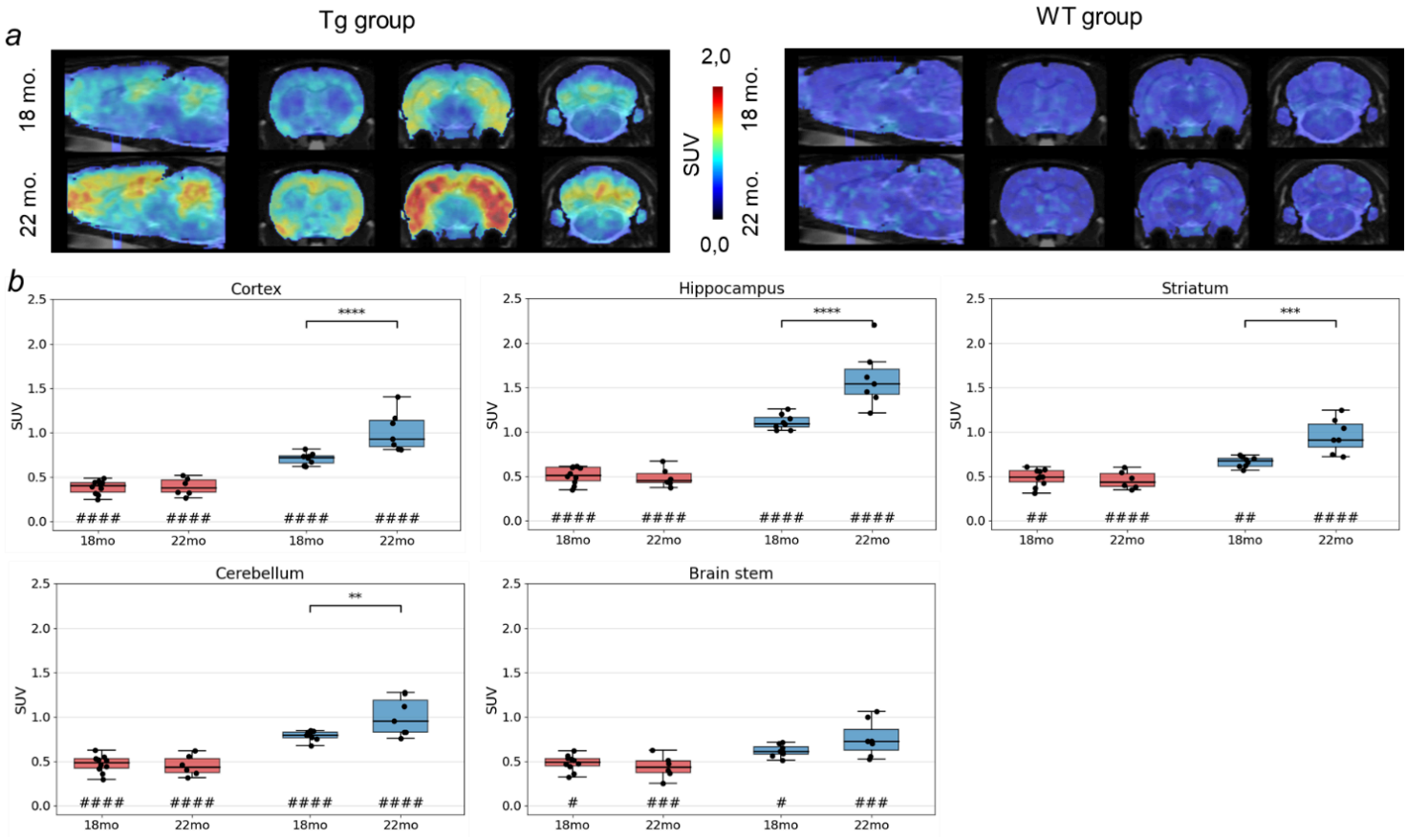

Figure 5

a) Longitudinal florzolotau (18F) SUV PET images obtained 65-90 min after injection in the Tg group and the WT group. Images correspond to the averaged PET image per time point and group (n = 7-8). b) SUV values in different brain regions for both animal groups (Tg:blue and WT: red) 65 to 90 min after tracer injection. Dots indicate individual animals. Stars (*) indicate statistical significance between time points within Tg or WT animals. Hash (#) indicates statistical significance between groups at each time point (*p, #p < 0,05; **p, ##p < 0,01; ***p, ###p < 0,001; ****p, #### < 0.0001).

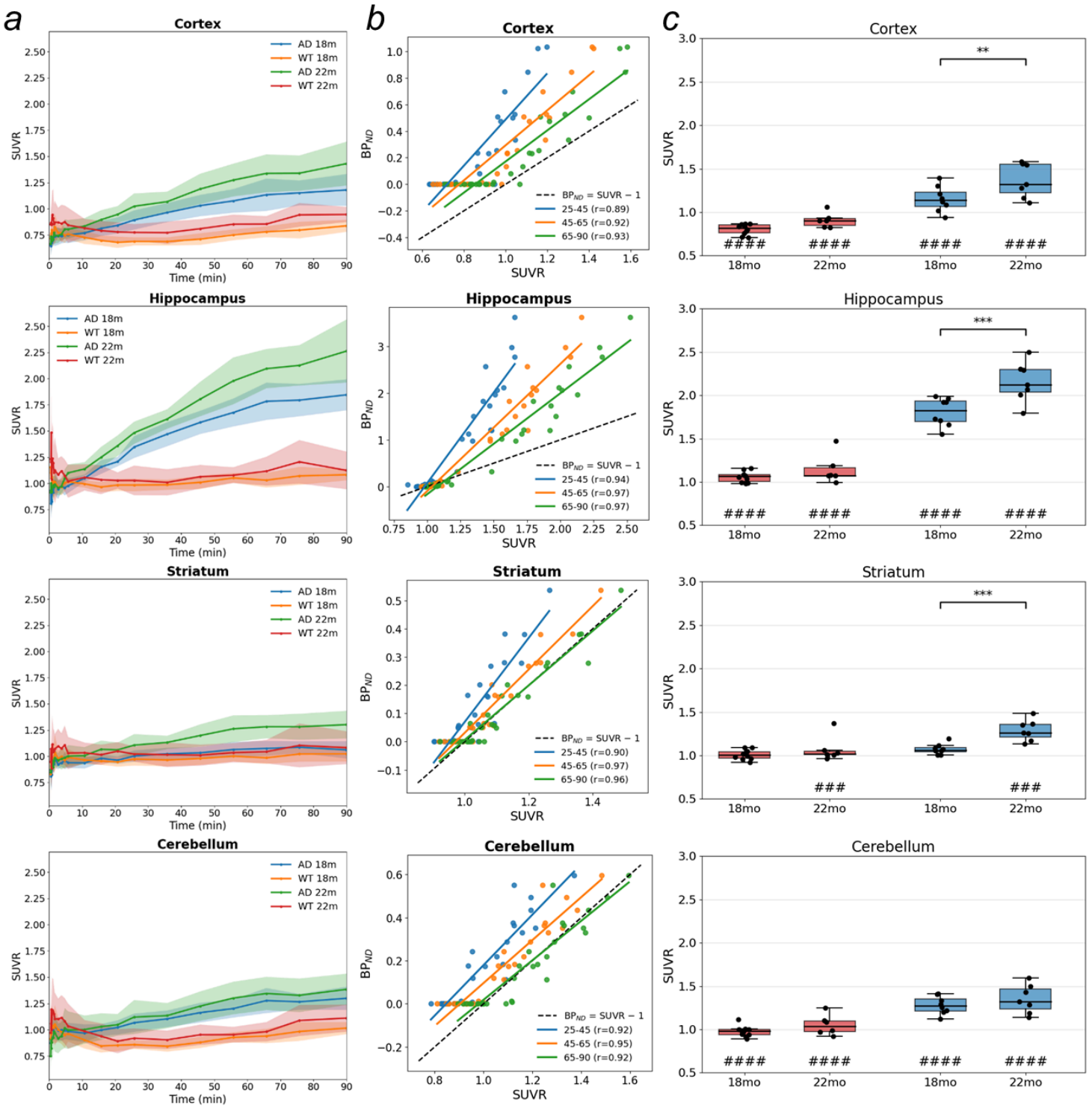

Figure 6

a) Time-activity curves of florzolotau (18F) SUVR in the cortex, hippocampus, striatum and cerebellum at 18 and 22 months of age for animals in Tg and WT groups. Brainstem as reference. Data are presented as mean ± SEM (standard error of the mean). b) Correlation between BP_{ND} and SUVR in three-time windows (25-45, 45-65, 65-90 min) in the cortex, hippocampus, striatum and cerebellum of Tg and WT animals (31 scans). Colour lines indicate regressions. Dashed black line indicates the theoretical identity relationship (BP_{ND} = SUVR − 1). c) florzolotau (18F) SUVR values in the cortex, hippocampus, striatum

and cerebellum for both animal groups (Tg: blue, WT: red) calculated 65-90 min post injection. Dots indicate individual animals. Stars (*) indicate statistical significance from 18 to 22 months within each group. Hash (#) indicates statistical significance between groups at each time point (**p < 0,01; ***p, ###p < 0,001; ####p, < 0.0001).

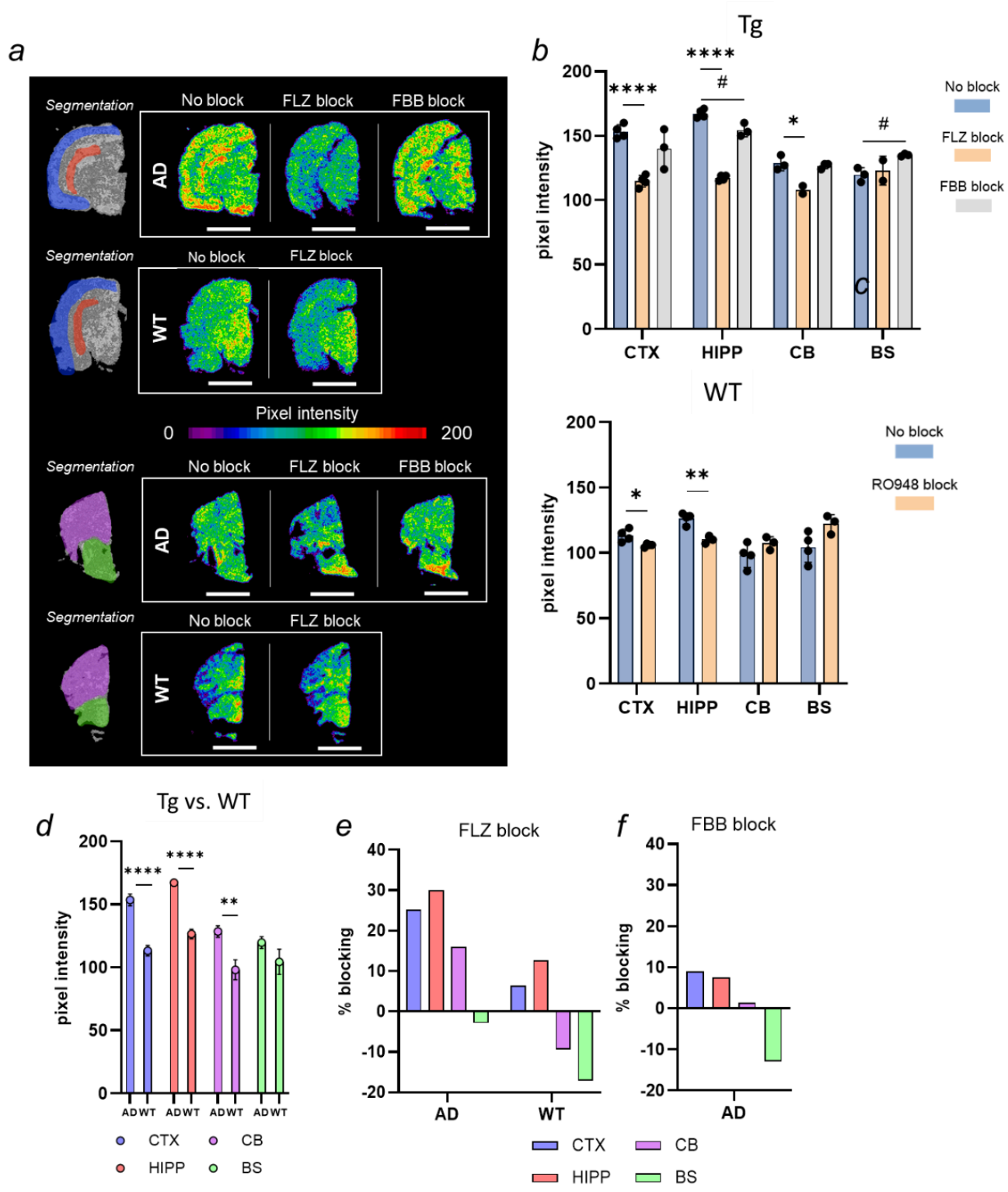

Figure 7

a) Representative coronal *in vitro* autoradiography images with florzolotau (18F) in Tg tissue (23 months, n =1) and WT tissue (22 months, n = 1). Manual segmentation is shown for clarity containing cortex (CTX, blue), hippocampus (HIPP, red), cerebellum (CB, purple) and brain stem (BS, green). Next to each slice is the corresponding blocked tissue: FLZ block (FLZ: Florzolotau) and FBB block (FBB: Florbetaben). Scale bar = 3 mm. Bar plots show tracer binding (mean pixel intensity values) in each region in different conditions: no blocking, FLZ blocking and FBB blocking for Tg (b) and WT tissue (c). Dots indicate experimental replicates with the same brain. Stars (*) indicate differences between no block and FLZ block. Hash (#) indicates differences between no block and FBB block. d) Differences in mean pixel intensity values (no block) between Tg and WT tissue. Bar plot showing the percentage of blocking (%) in each group and region for FLZ self-blocking (e) and FBB blocking (f). */#p < 0,05; **p < 0,01; ****p < 0,0001.